ADVANCED ELECTRONIC MATERIALS
www.advelectronicmat.de

Quantum Transport in Topological Surface States of Selectively Grown Bi_2Te_3 Nanoribbons

Daniel Rosenbach, Nico Oellers, Abdur Rehman Jalil, Martin Mikulics, Jonas Kölzer, Erik Zimmermann, Gregor Mussler, Stephany Bunte, Detlev Grützmacher, Hans Lüth, and Thomas Schäpers*

Quasi-1D nanowires of topological insulators are candidate structures in superconductor hybrid architectures for Majorana fermion based quantum computation schemes. Here, selectively grown Bi_2Te_3 topological insulator nanoribbons at cryogenic temperatures are investigated. The nanoribbons are defined in deep-etched Si_3N_4/SiO_2 nano-trenches on a silicon (111) substrate followed by a selective area growth process via molecular beam epitaxy. The selective area growth is beneficial to the device quality, as no subsequent fabrication needs to be performed to shape the nanoribbons. In the diffusive transport regime of these unintentionally *n*-doped Bi_2Te_3 topological insulator nanoribbons, electron trajectories are identified by analyzing angle dependent universal conductance fluctuation spectra. When the sample is tilted from a perpendicular to a parallel magnetic field orientation, these high frequent conductance modulations merge with low frequent Aharonov–Bohm type oscillations originating from the topologically protected surface states along the nanoribbon perimeter. For 500 nm wide Hall bars low frequent Shubnikov–de Haas oscillations are identified in a perpendicular magnetic field orientation. These reveal a topological, high-mobility, 2D transport channel, partially decoupled from the bulk of the material.

3D topological insulators (3D TIs) are a new class of materials that have a bulk electronic gap but highly conductive surface states, which promise a gapless, Dirac-like dispersion relation and spin-momentum locking of charge carriers occupying these surface states.[1,2] 3D TIs are candidates for a wide spectrum of applications, including the possible use for topology based quantum computation schemes.[3–5] In topological qubits the quantum state is decoded via the spatial arrangement of two Majorana zero modes (MZMs).[6] These arise, for example, in the vortex core of a type-II, *s*-wave superconductor at the interface toward a 3D TI[7] or at the interface of a quasi-1D nanowire of a 3D TI, proximitized by an *s*-wave superconductor.[8,9]

Conventional 3D TIs are the van der Waals bound, binary compounds such as Bi_2Te_3,[10] Bi_2Se_3,[11,12] Sb_2Te_3,[13] as well as alloys of these elements.[14,15] For a quasi 1D nanowire, due to the inclusion of the Berry-phase of a particle traversing the perimeter of the nanowire, the surface band structure is determined to be gapped.[16–18] By applying a magnetic flux parallel to the nanowire axis $\Phi = \pm\Phi_0/2$, where $\Phi_0 = h/e$, this gap will be closed. The non-degenerate, topologically protected linear surface bands will re-emerge periodically with a period of a full flux quantum $\Phi = (n + 1/2)\,\Phi_0$ threading the wire. The observation of such periodic Aharonov–Bohm (AB) oscillations has previously been reported.[19–24]

Making use of a selective area growth approach, nanowires of aforementioned materials can as well be deposited by molecular beam epitaxy (MBE).[25–28] These nanowires have a rather rectangular cross-section and are therefore referred to as nanoribbons. As a scalable bottom-up approach, these selectively grown nanoribbons are beneficial for desired Majorana surface architectures.[29] However, MBE grown 3D TI compounds usually

D. Rosenbach, N. Oellers, A. R. Jalil, J. Kölzer, E. Zimmermann, G. Mussler, D. Grützmacher, H. Lüth, T. Schäpers
Peter Grünberg Institut (PGI-9) Forschungszentrum Jülich
Jülich 52425, Germany
E-mail: d.rosenbach@fz-juelich.de

D. Rosenbach, N. Oellers, A. R. Jalil, J. Kölzer, E. Zimmermann, G. Mussler, D. Grützmacher, H. Lüth, T. Schäpers
JARA-Fundamentals of Future Information Technology
Jülich-Aachen Research Alliance
Forschungszentrum Jülich and RWTH Aachen University
Germany

The ORCID identification number(s) for the author(s) of this article can be found under https://doi.org/10.1002/aelm.202000205.

DOI: 10.1002/aelm.202000205

D. Rosenbach, G. Mussler, D. Grützmacher, T. Schäpers
Helmholtz Virtual Institute for Topological Insulators (VITI)
Forschungszentrum Jülich
Jülich 52425, Germany

M. Mikulics
Ernst Ruska-Centre for Microscopy and Spectroscopy with Electrons
Materials Science and Technology (ER-C-2)
Forschungszentrum Jülich
Jülich 52425, Germany

S. Bunte
Helmholtz Nano Facility (HNF)
Forschungszentrum Jülich
Jülich 52425, Germany

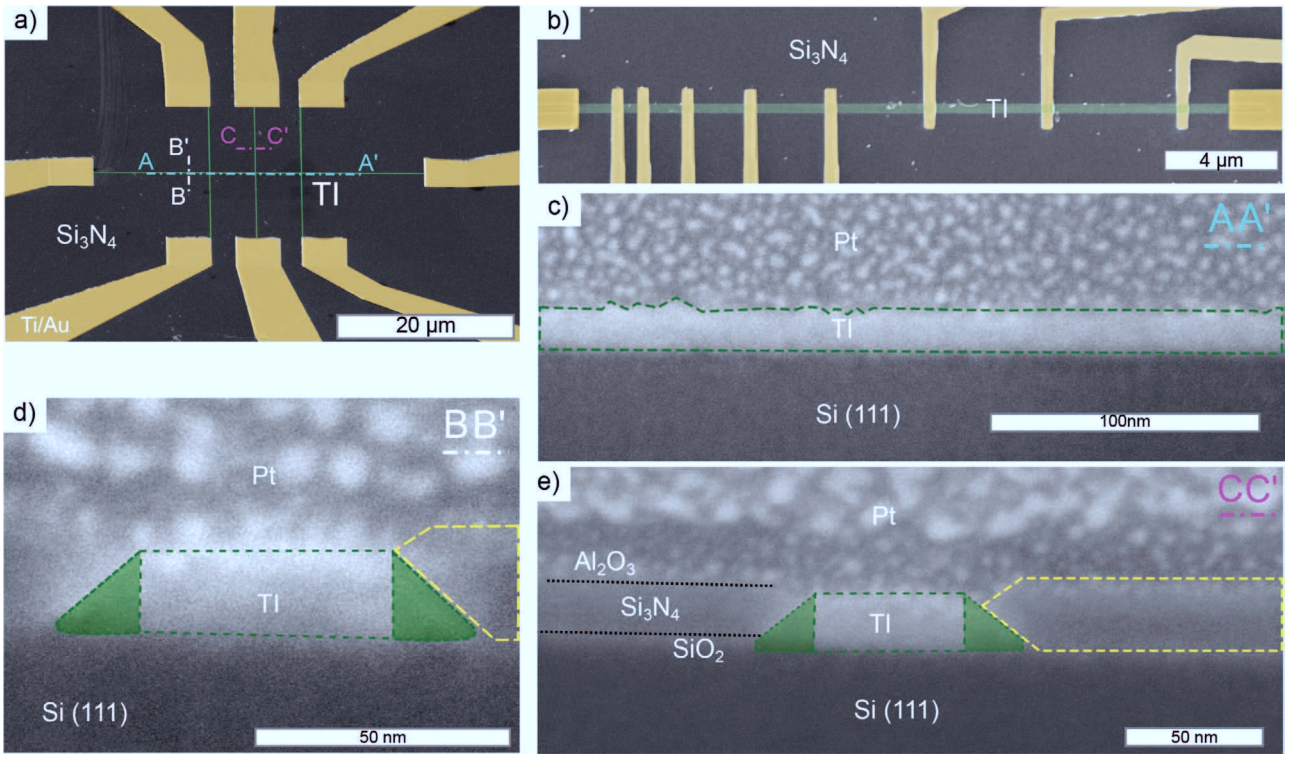

Figure 1. Selectively grown Bi_2Te_3 nanoribbon devices. Scanning electron micrographs of a) a 50 nm wide Hall bar and a b) 200 nm wide TLM nanoribbon. The devices are defined in deep-etched trenches within a layer stack of 20 nm Si_3N_4 on top of 5 nm SiO_2, that constitue the SAG mask. Planar Ti/Au (20 nm/50 nm) contacts have been deposited and are shown in gold/orange. In c)–e) three cross sections (AA′, BB′, and CC′) as indicated in a) of a 50 nm wide nanoribbon are shown, which are prepared using focused ion beam milling. The cross sections show the layer stack of the SAG mask and the Al_2O_3 capping layer. In c) thickness variations along the nanoribbon axis of $\Delta t \approx \pm 2$ nm can be identified. The cross sections in d) and e) have a trapezoidal shape, where the bottom surface of the TI layer is wider than on the top. Due to channeling effects during isotropic wet etching of the SiO_2, triangular pockets form below the Si_3N_4 layer. The TI continues to grow in these pockets, which are highlighted in shaded green. The Pt layer is deposited prior to ion beam milling.

suffer from a high unintentional background doping.[27,30] In such disordered nanoribbons with non-negligible bulk contributions $G \gg e^2/h$, the expected amplitude for the flux periodic oscillations in the cross section of the nanoribbon deviates from the simple periodic inclusion of the additional linear surface bands.[17,18] In bulk systems that exhibit strong spin-orbit coupling, the WAL effect is found to dominate the magnetoconductance oscillations.[31] The transition between rather bulk related, diffusive quantum interference modulations and quasi-ballistic surface related quantum transport has recently been reported in gate dependent measurements on etched HgTe nanoribbons.[32]

Here, Bi_2Te_3 nanoribbon based devices have selectively been grown and electrically characterized at cryogenic temperatures. The channel width ranges from 50 nm up to 500 nm. An Al_2O_3 capping has been applied to protect the topological surface states from degradation.[26,33] Characterization includes a detailed analysis of the magnetoconductance of nano-TLM and nano Hall bar devices. The transmission line method (TLM) devices are comprised of a single nanoribbon with terminals of varying contact separation lengths L, while Hall bar devices differ in width w. The magnetic field orientation was changed from an in-plane parallel orientation to a perpendicular out-of-plane orientation. In the perpendicular field orientation traceable universal conductance fluctuations (UCFs) have been identified. Performing Fast Fourier transformation and correlation field analysis on the magnetoconductance data the bulk phase coherence length has been determined. In the parallel field orientation, AB interference modulations have been identified that are restricted to the perimeter of the nanoribbons. The AB phase has also been observed for nanoribbons with a perimeter larger than the bulk phase coherence length. Furthermore, for a 500 nm wide nanoribbon, Shubnikov–de Haas (SdH) oscillations are identified at high magnetic fields. The 2D sheet carrier concentration as well as the mobility deduced from the SdH oscillations is superior to the bulk values obtained from Hall measurements. The highly mobile 2D sheet can be coined topological since a Berry phase offset of $\beta \sim \pi$ has been determined.

In **Figure 1**a,b selectively deposited TI devices are shown exemplarily. For comparison, investigated devices include µm scale as well as nm scale Hall bars and nanoribbons. For the selective area growth (SAG) mask, a SiO_2/Si_3N_4 layer stack on top of a Si(111) substrate is used. For details regarding the fabrication of the SAG mask, the reader is referred to the method section. In Figure 1c–e three cross sections of a 50 nm wide nanoribbon are shown (AA′, BB′, and CC′, as indicated in Figure 1a), which were prepared using focused ion beam milling. c) shows thickness fluctuations of $\Delta t \approx \pm 2$ nm along the nanoribbon. These occur during MBE deposition due to island growth. The cross sections perpendicular to the nanoribbon shown in d) and e) have a trapezoidal shape. Due to the

Table 1. Overview of the geometry of the five different nanoribbon devices investigated. The mean cross sectional areas $\bar{S}$ are determined and the expected AB frequencies are calculated. For comparison, the frequencies f determined from the FFTs performed as well as corresponding effective areas are displayed as well.

Device	$\bar{w}$ [nm]	$\bar{t}$ [nm]	$\bar{S}$ [nm^2]	$S\frac{e}{h}$[1/T]	f_{FFT}[1/T]	S_{FFT} [nm^2]
nHB-50	64	20	1280	0.31	0.34	1405
nHB-100	114	16.5	1881	0.50	0.38	1571
nHB-200	214	12.3	2632	0.72	0.46	1901
nHB-500	514	10	5140	1.24	–	–
nTLM-200	214	12.3	2632	0.72	0.45	1860

directional etching of the Si_3N_4 layer the top layer is slanted inward. The underlying SiO_2 etches isotropically in the hydrofluoric acid (HF) used for device preparation. Due to channeling effects of the HF within the nanotrench the Si_3N_4 layer is additionally slightly underetched. Within the underetched pockets (highlighted in green in Figure 1d,e) in the SiO_2 layer, the TI will continue to grow. Furthermore, it has been observed that for wider ribbon cross sections ($w > 100$ nm) the average film thickness is lower than that for less wide junctions. In the technique of selective area epitaxy the adatoms, depending upon their thermal mobility, diffuse laterally from the Si_3N_4 layer into the nanotrenches defined in the SAG mask. This will effectively change the growth rate of the material within the nanotrenches. This change in the growth rate has the inverse proportionality to the width of the trench, that is, the narrower the trench will be the faster it will grow. Therefore, the material within relatively thin nanotrenches has the tendency to grow thicker. In **Table 1** the mean thickness of nanoribbons of different widths are listed. These mean values exclude previously mentioned thickness variations along a single nanoribbon.

The TLM nanoribbon device has been used to study quantum modulations to the macroscopic magnetoconductance as a function of the device length L. A schematic overview as well as a scanning electron micrograph of the device are shown in **Figure 2**a. Analysis of the interface quality of applied Ti/Au contacts using the transmission line method[34,35] is discussed in the Supporting Information Section A. When a magnetic field is applied perpendicular to the nanoribbon, a sharp weak antilocalization (WAL) feature in between $-0.1\ \text{T} \leq B \leq +0.1$ T as well as additional universal conductance fluctuations (UCFs) for $B > \pm 0.1$ T are observed. The WAL effect as well as UCFs both originate from bulk interference of partial electron waves. Both effects can be used to determine the bulk phase coherence length l_ϕ.

In Figure 2b temperature-dependent magnetoconductance measurements on a $L = 950$ nm long segment of the nanoribbon are shown. Measurements have been performed in a four-terminal configuration. An FFT performed on the dataset obtained at 17 mK (as highlighted in blue in Figure 2c) shows several prominent frequencies. In the same graph FFTs performed on different segments of the nanoribbon are shown (highlighted in different shades of grey). See Section B, Supporting Information, for temperature-dependent magnetoconductance measurements on these other segments of the nanoribbon. Above 25 T^{-1}, no more prominent frequencies have been observed. Following $A = \Phi_0/B$, this threshold value corresponds to a maximum area of $A_{th} = 5.2 \times 10^{-14}$ m^2 that loops of phase-coherent transport span perpendicular to the applied magnetic field. The maximum area determined from the FFT, divided by the nanoribbon width w, gives an estimate of the phase coherence length l_ϕ along the ribbon for a channel width that is shorter than the phase coherence length l_ϕ. In fact $l_\phi \sim l = A_{th}/w = 260$ nm exceeds the junction width.

In order to determine l_ϕ more explicitly a temperature-dependent correlation field analysis of the form

$$F(\Delta B) = \langle \delta G(B + \Delta B)\delta G(B)) \rangle \quad (1)$$

on the same data is performed.[36–38] In the dirty limit, the relation between B_c and l_ϕ is expressed by $B_c(l_\phi) = \gamma \frac{e}{h}\frac{1}{w l_\phi}$, where the prefactor γ is chosen to be 0.42.[36] Results for the correlation fields B_c and the corresponding phase coherence lengths l_ϕ are shown in Figure 2d. Interestingly, l_ϕ at 17 mK coincides with the phase coherence length estimated from the FFT performed. l_ϕ does not increase anymore below $T \sim 2$ K. When considering only electron-electron interaction, the phase coherence length should increase even further for lower temperatures.[39] Scattering at the physical boundaries of the nanoribbon might be the reason that no increase of l_ϕ is observed. Width dependent nanoribbon measurements, performed at 1.5 K are discussed in the following.

Four nanoscale Hall bars have been electrically characterized at 1.5 K (exemplarily shown in Figure 1b). Hall bar dimensions are given in Table 1. Bulk sheet carrier density values are determined from Hall measurements to be in the range of $n_{2D} = (6.8 - 9.5) \times 10^{13}$ cm^{-2}. Similarly, bulk mobility values are determined to be in the range of $\mu = (307 - 374)$ cm^{2}Vs^{-1}. These values match with those measured on 1 µm and 10 µm wide selectively grown Hall bars. Therefore, the selectively grown Bi_2Te_3 3D TI nanoribbons deem the bulk to have a rather metallic character. See Section C, Supporting Information, for a detailed study of the Hall measurements.

Four-terminal magnetoconductance measurements on the nano Hall bars, however, show some distinct features when compared to the micrometer wide Hall bars. Longitudinal conductance measurements G_{xx} have been performed. **Figure 3**a.i–d.i (red curves) shows that an applied perpendicular magnetic field results in sharp WAL features with symmetric UCF modulations superimposed onto a mesoscopic background. A fit to the WAL feature as well as a correlation field analysis of UCFs is performed in order to determine the angle dependent phase coherence length l_ϕ for all Hall bars. Details are given in Section D, Supporting Information. In the correlation field analysis the phase coherence length for the 50 nm Hall bar is slightly reduced compared to the Hall bars of increased width. However, for Hall bars of $w \geq 100$ nm, the phase coherence length does not change anymore. Boundary scattering does not seem to limit the phase coherence length in nanoribbons of $w < l_\phi$ as previously assumed. A possible explanation for this upper limit of the phase coherence might be a potential increase at domain boundaries[40] or anti-phase boundaries due to steps on the surface of the substrate.[41,42] The average distance in between two step induced boundaries is approximately 250 nm.[43]

The Hall bars have been tilted from an effectively perpendicular magnetic field ($\Theta = 90°$, Figure 3a.i–d.i, red curves) to

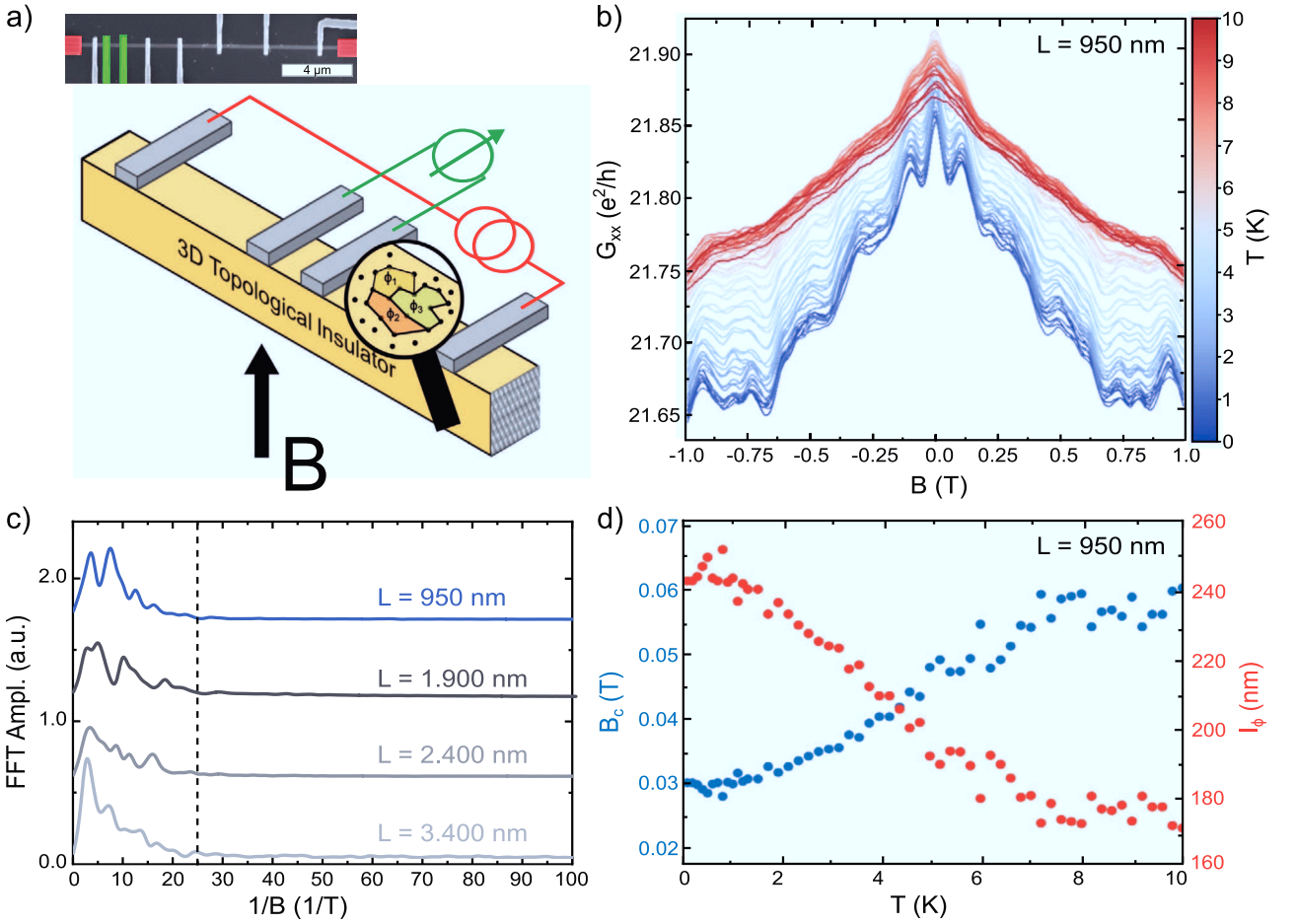

Figure 2. Nanoribbon with applied Ti/Au contacts of different contact separation length *L*. a) Schematic of the device layout. Measurements have been performed in a four-terminal setup (green: current bias, red: potential difference). b) Temperature dependent magnetoconductance measurements $G_{xx}(B)$ performed on a 950 nm long nanoribbon segment highlighted in (a). Phase coherent loops of quantum transport can be identified. c) Results of FFTs performed on the magnetoconductance G_{xx} on different segments of the nanoribbon. The blue curve highlights the FFT performed on the data at 17 mK base temperature shown in (b). d) Results of the correlation field B_c analysis, as well performed on the data at 17 mK base temperature shown in (b).

a field parallel to the current flow ($\Theta = 0°$, Figure 3a.i–d.i, blue curves). The magnetoconductance measurements performed with a stepping of $\Delta\Theta = 2°$ show a systematic change in the modulation pattern. This systematic change becomes more evident in the background-subtracted magnetoconductance data ΔG_{xx}, as shown in Figure 3a.ii–d.ii. The quantum modulation peaks are found to follow a sinusoidal behavior as a function of the tilt angle Θ. This behavior is even more prominent in maps of the FFT amplitude as a function of frequency ($1/B$) and tilt angle (Θ) (shown in Figure 3a.iii–d.iii). These loops are projections of any complex 3D electronic path onto the relevant 2D plane, perpendicular to the applied magnetic field.[36]

For interference paths, that would solely expand on a 2D plane, the maximum observed frequency $1/B$ lies at exactly $\Theta = 90°$. At a 90° offset from that maximum frequency, the effective flux through the 2D interference loops should be 0. In the measured data, the maximum at $\Theta = 90°$ is observed, however, at $\Theta = 0°$ quantum modulations with finite frequency are still present. The reason therefore is that at low angles Aharonov–Bohm (AB) type oscillations are expected to originate from the topologically protected surface states on the perimeter of the nanoribbon.[19–24] At low angles ($\Theta \leq 10°$) both AB type oscillations as well as UCFs merge.[24,44] Similar results have been observed on the TLM nanoribbon structure. See Section E, Supporting Information, for a discussion of the angle dependent measurements on the TLM nanoribbon. The AB type modulations to the magnetoconductance are analyzed in the following.

AB type modulation features at small angles $\Theta \leq 10°$ are observed in the nano TLM and the nano Hall bar structures. The expected frequencies ($f = 1/B$) for interference after traversing the whole nanoribbon perimeter $S = S_{xy,max}$ are determined using $f = eA/h$. An overview of the expected AB oscillation frequencies is given in Table 1. AB type oscillations at magnetic fields applied along the nanoribbon axis have been identified for the 50 nm (nHB-50), 100 nm (nHB-100), and 200 nm (nHB-200) wide Hall bars as well as for the 200 nm wide TLM nanoribbon segments (nTLM-200). No AB type oscillations have been identified for the 500 nm wide Hall bar (nHB 500).

In order to isolate the AB oscillations ($\Delta G_{xx}(B_z)$) from the macroscopic magnetoconductance a smooth background has been subtracted by applying a first order Savitzky–Golay filter.

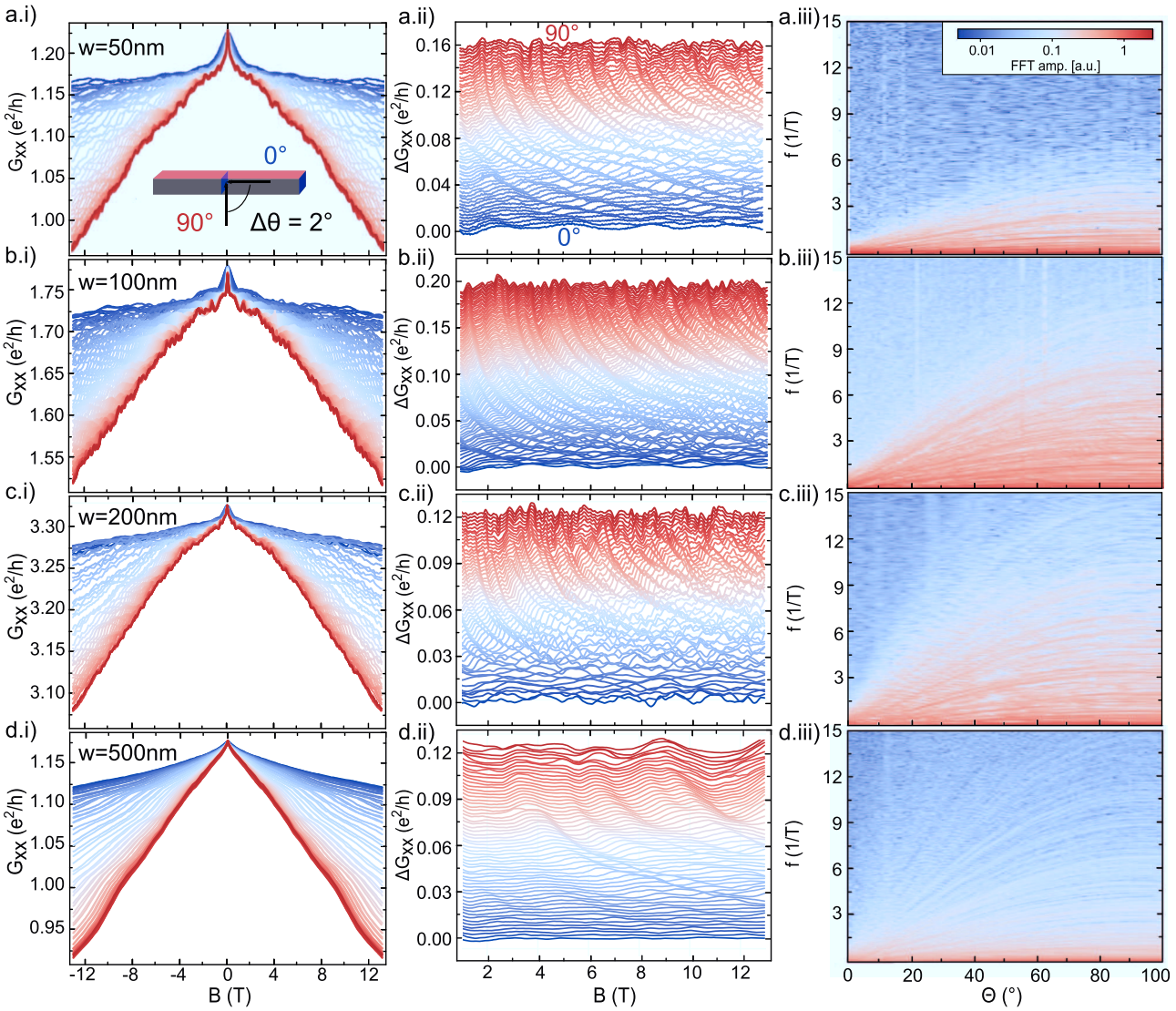

Figure 3. Angle dependent measurements performed on the selectively grown Bi_2Te_3 nano Hall bars of different width w. a.i)–d.i) Angle dependent magnetoconductance measurements. The red curves show the magnetoconductance behavior at an effectively perpendicular out-of-plane magnetic field and the blue curves at an effectively parallel in-plane magnetic field as shown in the schematic in a.i). The gradient in color in between the red and blue curves show intermediate angles. a.ii-d.ii) show the magnetoconductance values after subtraction of an averaging background. For clarity, only positive magnetic field values, excluding the WAL feature below 1 T, are plotted. a.iii)–d.iii) FFT amplitude as a function of tilt angle and frequency. The FFT is performed on the whole data range of $-13\,\mathrm{T} \leq B \leq +13\,\mathrm{T}$.

The results are shown in **Figure 4**a–d. The prominent features in between $-1\ \mathrm{T} \leq B \leq +1\ \mathrm{T}$ are explained by the WAL effect. Outside this range the different curves all show a distinct oscillatory behavior. Prominent oscillation periods are highlighted within each graph. FFT results on each data set are shown in the respective inset. The amplitude of the frequency count, normalized to the greatest amplitude determined, is displayed as a function of the frequency $1/B$. The most prominent frequencies are marked in every graph.

The 50 nm Hall bar shows a frequency count with greatest amplitude at $f = 1/B = 0.34\ \mathrm{T}^{-1}$ ($\Delta B = 2.94$ T). The corresponding area measures $e/hB = 1280\ \mathrm{nm}^2$. For the 100 nm Hall bar two prominent frequencies are observed at $f = 0.27\ \mathrm{T}^{-1}$ ($\Delta B = 3.70$ T, $e/hB = 1116\ \mathrm{nm}^2$) and at $f = 0.38\ \mathrm{T}^{-1}$ ($\Delta B = 2.63$ T, $e/hB = 1571\ \mathrm{nm}^2$). Prominent frequencies observed for the 200 nm Hall bar are $f = 0.35\ \mathrm{T}^{-1}$ ($\Delta B = 2.86$ T, $e/hB = 1447\ \mathrm{nm}^2$) and at $f = 0.46\ \mathrm{T}^{-1}$ ($\Delta B = 2.17$,T, $e/hB = 1901\ \mathrm{nm}^2$). The areas determined using FFT can be compared to the geometrically identified areas. The geometrically identified areas $\overline{S}$ (Table 1, 4th column) of the 50 nm and 100 nm wide ribbon matches the effective area determined from the frequencies in the FFT analysis performed on the AB magnetoconductance oscillations S_{FFT} (Table 1, seventh column). The geometrically determined area of the 200 nm wide ribbon seems to be overestimated, when compared to S_{FFT}. However, the determined frequency of the AB oscillations within both the 200 nm wide Hall bar and the 200 nm wide TLM device $f = 0.45\ \mathrm{T}^{-1}$ ($\Delta B = 2.22$ T, $e/hB = 1860\ \mathrm{nm}^2$) match. A possible explanation for this

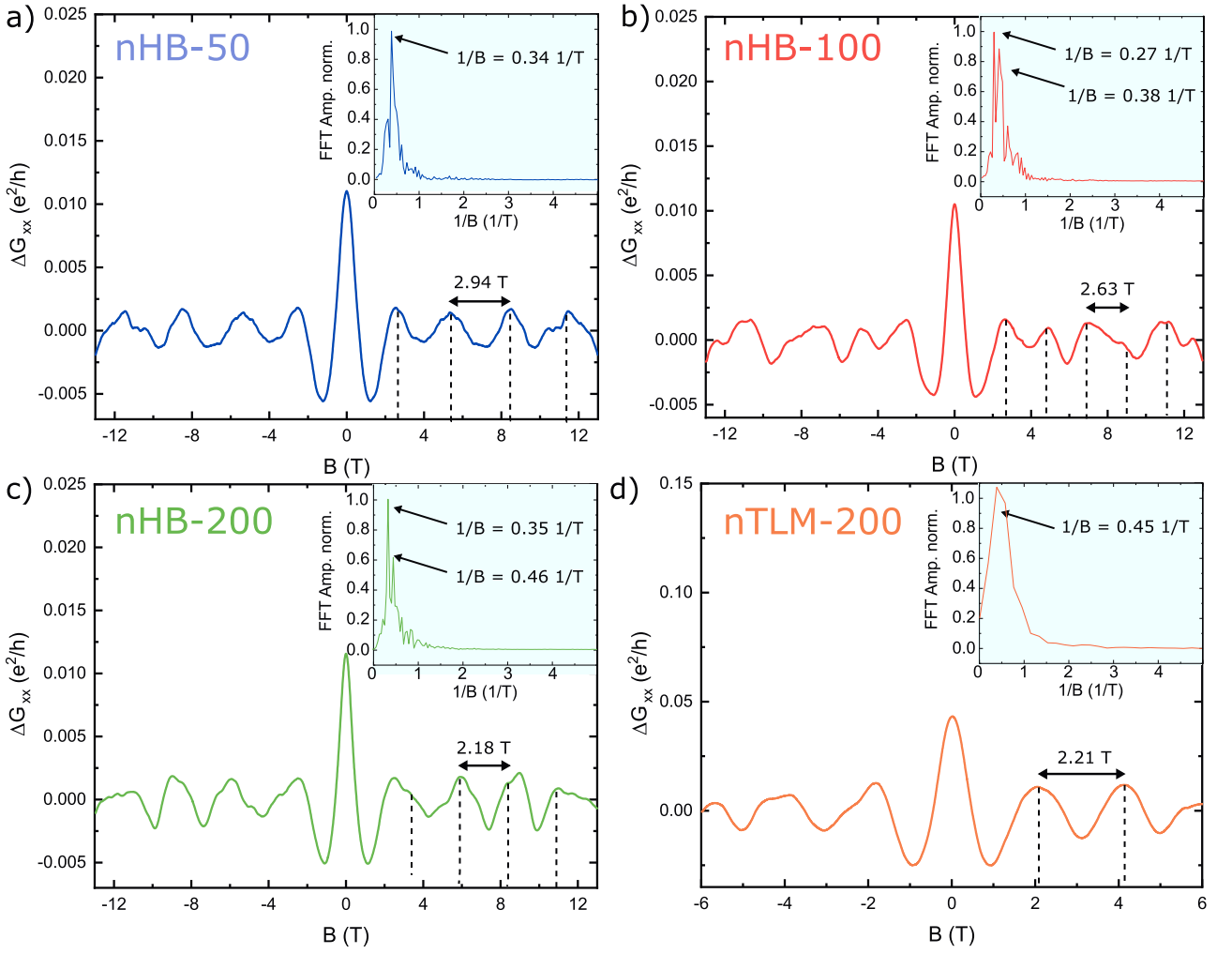

Figure 4. Magnetoconductance measurements in a magnetic field applied along the nanoribbon axis. The a) 50 nm (nHB-50), b) 100 nm (nHB-100) and c) 200 nm wide Hall bar (nHB-200), as well as one of the d) 200 nm (nTLM-200). wide nano TLM ribbon segments, are compared. A smooth background has been subtracted and the change in conductance $\Delta G_{xx}(B)$ is shown. For $B > \pm 1$ T several pronounced AB oscillation periods can be identified. An FFT is performed and shown in the inset of each figure. In the FFT peaks with highest amplitude are identified and frequencies in $1/B$ mentioned.

systematic deviation might be that the actual penetration depth of the wave function in the topological surface states needs to be considered.[46] The penetration depth thereby measures 1–2 nm. Especially for thin and wide cross sections the effective area will change.

The prominent frequencies determined from the FFT analysis on the magnetoconductance data highlight the existence of AB oscillation patterns originating from only a few fixed loop sizes in the nanoribbon cross sections. The largest amplitude is observed for frequencies that correspond to loop sizes matching the cross sectional area of the nanoribbons. The perimeter of the 200 nm wide Hall bar however exceeds the previously determined phase coherence length ($U_{100\,\mathrm{nm}} \approx 261$ nm $< l_\phi < U_{200\,\mathrm{nm}} \approx 453$ nm). A possible explanation might be an additional transport channel on the perimeter of the nanoribbon with a phase coherence length of at least 453 nm, that is partially decoupled from the bulk. The perimeter of the 500 nm wide ribbon ($U_{500\,\mathrm{nm}} \approx 1048$ nm). however, seems to exceed even this increased phase coherence length on this TI surface, since no AB oscillations have been observed. It is not unambiguously distinguishable, whether these oscillations originate from topological surface states or classical two-dimensional surface states that results from band bending effects.[46] A distinction can be drawn by extracting the Berry phase from Shubnikov–de Haas oscillations.[47] Consequently, Shubnikov–de Haas (SdH) oscillations observed in a magnetic field applied perpendicular out-of plane are analyzed and discussed in the next section.

The angle dependent magnetoconductance of the 500 nm wide Hall bar shows some distinctive features, when compared to the 50, 100, and 200 nm wide Hall bars. In the out-of plane perpendicular field orientation, high frequency UCF spectra are observable in the FFT analysis (Figure 3d.iii) but with reduced relative amplitude. Additionally, low-frequency SdH oscillations are observed in the perpendicular field orientation at high magnetic fields $B \geq 4$ T. In the $\Delta G_{xx}(B, \Theta)$

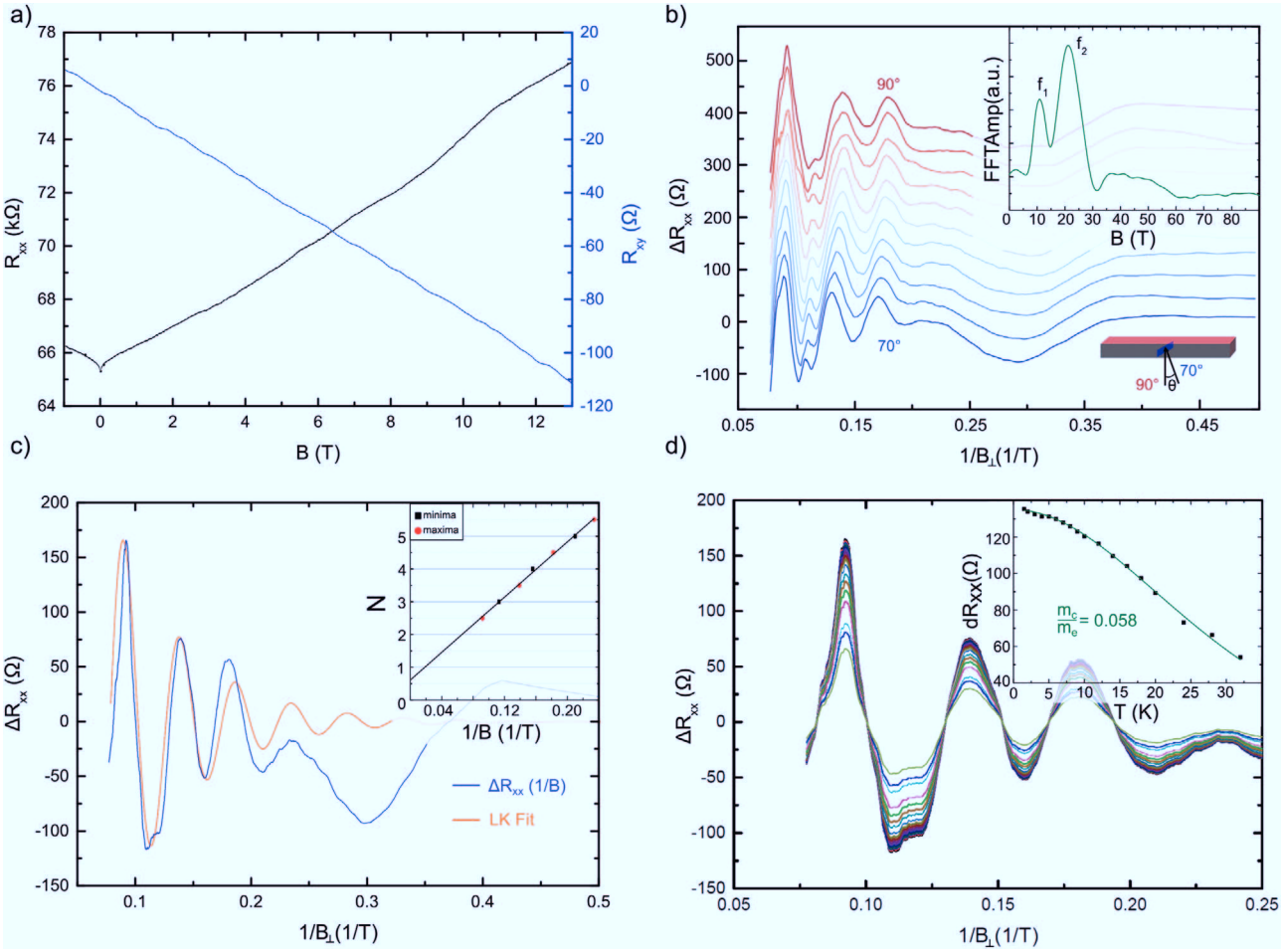

Figure 5. Low frequent SdH-oscillations observed for the 500 nm wide Hall bar (nHB-500). a) Longitudinal R_{xx} (black curve) as well as Hall resistance R_{xy} (blue curve) measured at $\Theta = 90°$. b) Magnetoresistance oscillations are plotted after background subtraction as a function of the inverse perpendicular magnetic field $\Delta R_{xx}(B_\perp$ for angles in between $70° \leq \Theta \leq 90°$). The FFT shown in the inset is performed on the $\Theta = 90°$ sweep and shows two prominent frequencies $f_1 = 11.3$ T and $f_2 = 21.7$ T. c) The general LK expression (orange curve) is fitted to the SdH-oscillations (blue curve) to extract mobility $\mu = 1997.3 \frac{cm^2}{V \cdot s}$ and phase-offset $\beta_{LK} = 0.508$. In the inset of c) the maxima and minima in the SdH-oscillations are plotted against the inverse magnetic field as half integer and full integer Landau levels N, respectively. The linear fit performed is used to extract the y-intercept (phase-offset $\beta_{LL} = 0.612$). d) Temperature dependent SdH-oscillations pattern. The oscillation amplitude at $1/B = 0.09211/T$ is plotted in the inset as a function of temperature. A fit based on the thermodynamic part of the Lifshitz-Kosevich expression is used to extract the cyclotron frequency $\omega_c = 3.19 \times 10^{13}$ 1/s.

dataset (Figure 3d.ii) it is evident, that the SdH oscillations originate from a 2D sheet parallel to the sample surface.

In **Figure 5**a the longitudinal resistance $R_{xx}(B)$ for an applied magnetic field perpendicular ($\Theta = 90°$) to the 500 nm wide nanoribbon is shown. $R_{xx}(B)$ is displayed together with the Hall voltage $R_{xy}(B)$. A smooth background using a Savitzky–Golay filter is subtracted from the longitudinal magnetoresistance $R_{xx}(B)$ curve. The result is shown as a function of the inverse magnetic field $\Delta R_{xx}(1/B)$ in Figure 5b (dark red curve) and shows periodic SdH magnetoresistance modulations. $\Delta R_{xx}(1/B_\perp)$ values are displayed for various tilt angles in between $70° \leq \Theta \leq 90°$. For the angle dependency of the SdH-oscillations only the perpendicular magnetic field component ($B_\perp = B \cdot \sin\Theta$) has been considered. The observed oscillation period does not shift upon changing the angle Θ. The FFT performed on the curve at $\Theta = 90°$ (Figure 5b, insert) shows two distinct frequencies $f_1 = 11.3$ T and $f_2 = 21.7$ T. The second frequency matches the period observed in the $\Delta R(1/B_\perp)$ magnetoresistance curve. Oscillation frequency f_1 relates to the same oscillations with doubled period. Using the Onsager relation $f = e/2n_{SdH}\pi\hbar$,[27] with $f = f_2$ being the frequency of the SdH-oscillations, we extract a 2D sheet carrier concentration of $n_{SdH} = 5.31 \times 10^{11}$ cm^{-2}, for $f = f_2 = 21.7$ T. This value is about two orders of magnitude smaller than the 2D sheet carrier concentration determined from Hall measurements performed. Results show that there is an additional transport channel, which is partially decoupled from the bulk.

A Lifshitz–Kosevich (LK) expression[48–50] of the form,

$$\Delta R_{xx} = a \cdot e^{-\pi/\mu \cdot B} \cdot \cos\left(2\pi \cdot \frac{f}{B} + \pi + \beta_{LK}\right) \quad (2)$$

is used to fit $\Delta R_{xx}(1/B_\perp)$ (see Figure 5c, pink curve). In the equation above a is the oscillation amplitude, μ is the mobility, $f = f_2$ is the oscillation period and β_{LK} is the phase-offset. In the fit performed μ and β are used as fit parameters and results in a mobility value of $\mu_{\mathrm{SdH}} = 1997.3 \frac{\mathrm{cm}^2}{\mathrm{V \cdot s}}$ and a phase offset of $\beta_{LK} = 0.507$. The mobility μ_{SdH} is found to be about a factor of 5 larger than the bulk mobility determined $\mu_{bulk} = 374 \frac{\mathrm{cm}^2}{\mathrm{V \cdot s}}$.

In order to identify the origin of the two-dimensional transport channel with higher mobility μ and lower sheet carrier concentration n the physically relevant phase-offset β_{LK} extracted from the LK-fit is considered. For a classical 2D electron gas in an accumulation space charge layer the expected phase-offset would be zero. A deviation from that value has been reported to be the case in linear Dirac systems due to the Berry phase.[47] The spin-momentum locking present in the TIs leads to a Berry phase offset of π for a charge traversing one full circle in k-space. A phase-offset of π in SdH analysis has already been reported for other Dirac systems as well.[48,50] The Landau level index N is plotted against the inverse perpendicular magnetic field $1/B_\perp$ in the inset of Figure 5c. In total seven extrema have been identified that match the oscillatory pattern of frequency $f = 21.7$ T. The minima are addressed as full integer Landau level steps, while the maxima are addressed as half integer Landau level steps. The phase-offset β_{LL} has been identified by interpolating the Landau level fan diagram in order to determine the y-intercept. The phase-offset extracted from the interpolated line is $\beta_{LL} = 0.612$, which is in good agreement with the phase-offset extracted from the LK fit ($\beta_{LK} = 0.507$). Thus, it is plausible that the 2D transport channel indeed originates from topological surface states.

By assuming a linear dispersion for the topological surface states identified as $E = v_F k\hbar$ the Fermi energy can be deduced from the oscillatory frequency of the SdH-oscillations following the relation

$$E_F = \sqrt{f_2 \cdot v_F^2 \cdot 2e \cdot \hbar}, \tag{3}$$

where $f_2 = 21.7$ T and v_F is the Fermi velocity. In order to determine the Fermi velocity v_F, the Dirac dispersion relation $\delta E/\delta k = v_F\hbar$ as well as the general expression for the cyclotron mass $m_c = k_F\hbar^2(\delta E/\delta k)^{-1}$ is used. The Fermi wave vector is given by $k_F = \sqrt{4\pi n_{SdH}} = 2.58 \times 10^8$ m^{-1}, assuming a 2D space. The cyclotron mass has been obtained from a fit based on the temperature dependent part of the LK expression[27] to the temperature dependent oscillation amplitude of the SdH-oscillations. In Figure 5d $\Delta R_{xx}(1/B_\perp)$ for various temperatures $1.5\,\mathrm{K} \le T \le 30\,\mathrm{K}$ is shown. The oscillation amplitude of the first maxima at $1/B_\perp = 0.0921\,1/T$ is plotted as a function of temperature in Figure 5d (insert). The values for the best fit obtained result in $\omega_c = 3.19 \times 10^{13}$ s^{-1}. The cyclotron mass is then given by $m_c = e \cdot B/\omega_c = 5.451 \times 10^{-32}$ kg, at $B = 1/0.0921\,T = 10.86\,T$, which is the position of the first SdH maximum. With these values the Fermi velocity has been determined to be $v_F = \hbar k_F/m_c = 5.08 \times 10^5\,\mathrm{ms}^{-1}$. The position of the Fermi energy, with reference to the Dirac point (DP) is evaluated using Equation (3) and results in $E_F - E_{DP} = 86$ meV. Previously reported angle resolved photoemission spectra (ARPES) of bulk samples of Bi_2Te_3[51] show that the Fermi energy is located slightly above the bulk conduction band minimum ($E_F - E_{DP} = 300 \pm 10$ meV). The Fermi energy position determined here, however, locates the Fermi energy slightly above the bulk valence band edge. ARPES probes only the top surface of the TI, while a different band alignment at the bottom surface toward the substrate can change the relative position of the Fermi energy to the bottom Dirac cone. Results presented here point to the possibility that observed SdH oscillations originate from the bottom surface of the nanoribbon. Similar observations regarding the band positions on the bottom surface of MBE grown $(Bi,Sb)_2Te_3$ thin films have been reported by Lüpke et al. during scanning tip potentiometry measurements.[52]

The determined sheet carrier concentration on the bottom surface compares well to previously reported values on p-type Bi_2Te_3 single crystals[53] as well as Bi_2Te_3 nanowires.[54] In vapour deposited Bi_2Se_3 nanowires the sheet carrier concentration is slightly increased.[55] Earlier reports show, that SdH oscillations from two different 2D subsystems in Bi_2Te_3 nanowires could be distinguished.[54,56] The extracted charge carrier densities from both subsystems have been in the same order of magnitude. From ARPES measurements on the top surface of MBE grown Bi_2Te_3 thin films[51] a sheet carrier concentration of $n_{\mathrm{top}} = 1.8 \times 10^{13}$ cm^{-2} can be deduced, which is two orders of magnitude higher than the sheet carrier concentration of the bottom surface determined here. This difference in the charge carrier concentration explains why only SdH oscillations from charges on the bottom surface have been identified here.

We investigated selectively grown Bi_2Te_3 nanoribbons and nano Hall bars of varying width in low temperature electrical transport studies. Different quantum transport phenomena have been identified in magnetoconductance measurements. The focus has been set to understand, which of these quantum modulation phenomena can be attributed to the bulk of these diffusive nanoribbons and which to the topologically protected surfaces.

TLM measurements have been performed on nano- as well as microribbons with Ti/Au contacts in order to evaluate the contact resistance for different contact areas. It has been concluded that even though the contact area for the nanoribbon devices is just a small fraction of the contact area provided for the microribbons ($S_{c,\mathrm{micro}}/S_{c,\mathrm{nano}} = 2.500$), the contact resistance is not increased significantly. The sheet resistance as well as the specific bulk resistivity for different ribbon-dimensions has been determined. Including Hall bar measurements performed on both nano- as well as microribbons it can be concluded that the TI ribbon properties, with respect to bulk resistivity, bulk sheet carrier concentration, as well as bulk mobility shows no dependency on geometry.

By evaluating WAL features and UCF spectra the bulk phase coherence length along the nanoribbon was determined to be $l_\phi = 240$ nm. For an out-of plane perpendicular magnetic field this results in traceable defect based coherent electron interference loops, which are limited in one direction by the nanoribbon width. By performing angle-dependent magnetoconductance measurements, these interference loops have been determined to reside on two-dimensional planes parallel to the sample surface, mainly originating from the bulk. For a

magnetic field parallel to the nanoribbon axis, AB type oscillations have been determined that can be attributed to an additional, highly coherent transport sheet on the circumference of the nanoribbons, that is partially decoupled from the bulk. The angle dependent magnetoconductance measurements furthermore show how the UCFs and the AB type oscillations merge at low angles. The UCF spectra dominate for $\Theta > 10°$, while the AB type oscillations dominate for $\Theta \leq 10°$. For the 500 nm wide nanoribbon, Shubnikov–de Haas oscillations have been observed. The deduced sheet carrier density is lower and the mobility higher, when compared to the bulk values determined. A Lifshitz–Kosevich fit to the SdH oscillation period in the inverse perpendicular magnetic field has been performed. The phase-offset determined from this fit coincides with the phase-offset determined by analyzing individual Landau levels and measures $\beta \sim \pi$. This phase offset of nearly π is a clear indication of the Berry phase, which is only present in topological surface states.

The analysis performed shows that the selectively grown Bi_2Te_3 nanoribbons suffer from a high bulk carrier density and a low bulk mobility. However, convincing signatures of surface state transport, superimposed onto bulk effects, have been found. Especially compared to nanoribbons and nanowires prepared by other means, the MBE grown TI nanoribbons analyzed here have an increased bulk conduction and much stronger coupling in between the bulk and the respective topological surface(s). The characterization tools presented here can be used to further study the behavior of selectively grown 3D TI nanoribbons of improved quality and more bulk insulating properties. The bulk behavior can further be suppressed in future devices by including electrostatic gating. The main advantage of using the MBE grown nanoribbons is the scalability of the SAG process used. In combination with bulk insulating nanoribbons this will allow for large scale investigation of two-dimensional TI nanoribbon architectures[26] and can ultimately be included into topological insulator-superconductor hybrid devices, for the realization of quantum computation schemes based on Majorana fermions.

Experimental Section

Mask Fabrication and Selective Area Growth: TI nanoribbon structures were grown by MBE following a selective-area growth (SAG) approach. The first 5 nm of a Si(111) 2000-$\Omega \cdot$ cm wafer were thermally converted into SiO_2. Subsequently a 20 nm thick Si_3N_4 layer was deposited via low-pressure chemical vapor deposition. The desired structures were defined using electron beam lithography. Using reactive ion etching (CHF_3/O_2 gas mixture) and hydrofluoric acid wet etching, the Si_3N_4 and the SiO_2 layers were etched, respectively. Thus the Si(111) surface was locally revealed. The structured Si_3N_4/SiO_2 layers therefore formed the SAG mask.

The standard parameters for selective growth of Bi_2Te_3, given a substrate temperature of $T_{sub} = 300\,°C$, a Bi-cell temperature of $T_{Bi} = 470\,°C$, and a Te-cell temperature of $T_{Te} = 325\,°C$, resulted in a growth rate of 7 nm/h. The TI films were grown in the Te-overpressure regime.

Electrical Measurement Setup: Ohmic Ti/Au contacts were deposited in a vacuum chamber by means of thermal evaporation. Magnetotransport measurements were performed in a $^3He/^4He$ dilution refrigerator with a base temperature of 17 mK and a ^4He variable temperature insert (VTI) cryostat with a base temperature of 1.5 K. The dilution refrigerator provided magnetic fields of up to 6 T perpendicular out-of plane and up to 1 T parallel and perpendicular in-plane. The maximum magnetic field provided in the VTI measured 13 T. The sample rod for the VTI cryostat was equipped with a rotatable substrate holder to rotate the sample with respect to the static magnetic field. Two- as well as four-terminal measurements were performed using standard a.c. lock-in techniques for current injection.

Supporting Information

Supporting Information is available from the Wiley Online Library or from the author.

Acknowledgements

The authors would like to thank Gunjan P. Nagda for a critical review of contents and proof reading of the manuscript. The authors would like to thank Herbert Kertz for the technical supervision of the experimental setups. This work was financially supported by the Virtual Institute for Topological Insulators (VITI), which is funded by the Helmholtz Association. This work was partly funded by the Deutsche Forschungsgemeinschaft (DFG, German Research Foundation) under Germany's Excellence Strategy – Cluster of Excellence Matter and Light for Quantum Computing (ML4Q) EXC 2004/1 – 390534769.

Conflict of Interest

The authors declare no conflict of interest.

Author Contributions

D.R. initiated the project and performed measurements on the nano-TLM and nano Hall bar devices. N.O. performed measurements on micrometer sized TLM and Hall bar devices. D.R. and A.R.J. have been fabricating the devices in clean room conditions. A.R.J. and G.M. have deposited the selectively grown nanoribbon structures. M.M. and N.O. have been designing the nano- and micro-TLM devices. D.R., J.K., and E.Z. have maintained the operation of the cryogenic setups, the electrical measurement devices and the python based measurement scripts. D.R. and S.B. have performed the focused ion beam cut as well as the micrographical analysis of the nanoribbon cross sections. The project has been supervised by and intensively discussed with D.G., H.L., and Th.S.

Keywords

molecular beam epitaxy, nanofabrication, nanoribbons, quantum transport, selective area growth, topological insulators

Received: February 25, 2020
Revised: June 9, 2020
Published online:

[1] L. Fu, C. L. Kane, E. J. Mele, *Phys. Rev. Lett.* **2007**, *98*, 106803.
[2] Y. Ando, *J. Phys. Soc. Jpn.* **2013**, *82*, 102001.
[3] L. Fu, C. L. Kane, *Phys. Rev. Lett.* **2008**, *100*, 096407.
[4] J. Manousakis, A. Altland, D. Bagrets, R. Egger, Y. Ando, *Phys. Rev. B* **2017**, *95*, 165424.

[5] T. Hyart, B. van Heck, I. C. Fulga, M. Burrello, A. R. Akhmerov, C. W. J. Beenakker, *Phys. Rev. B* **2013**, *88*, 035121.
[6] C. Nayak, S. H. Simon, A. Stern, M. Freedman, S. Das Sarma, *Rev. Mod. Phys.* **2008**, *80*, 1083.
[7] H.-H. Sun, K.-W. Zhang, L.-H. Hu, C. Li, G.-Y. Wang, H.-Y. Ma, Z.-A. Xu, C.-L. Gao, D.-D. Guan, Y.-Y. Li, C. Liu, D. Qian, Y. Zhou, L. Fu, S.-C. Li, F.-C. Zhang, J.-F. Jia, *Phys. Rev. Lett.* **2016**, *116*, 257003.
[8] A. Cook, M. Franz, *Phys. Rev. B* **2011**, *84*, 201105(R).
[9] F. de Juan, R. Ilan, J. H. Bardarson, *Phys. Rev. Lett.* **2014**, *113*, 107003.
[10] J. Krumrain, G. Mussler, S. Borisova, T. Stoica, L. Plucinski, C. Schneider, D. Grützmacher, *J. Cryst. Growth* **2011**, *324*, 115.
[11] H. M. Benia, C. Lin, K. Kern, C. R. Ast, *Phys. Rev. Lett.* **2011**, *107*, 177602.
[12] G. Zhang, H. Qin, J. Chen, X. He, L. Lu, Y. Li, K. Wu, *Adv. Funct. Mater.* **2011**, *21*, 2351.
[13] Y. Takagaki, A. Giussani, K. Perumal, R. Calarco, K.-J. Friedland, *Phys. Rev. B* **2012**, *86*, 125137.
[14] J. Zhang, C.-Z. Chang, Z. Zhang, J. Wen, X. Feng, K. Li, M. Liu, K. He, L. Wang, X. Chen, Q.-K. Xue, X. Ma, Y. Wang, *Nat. Commun.* **2011**, *2*, 574.
[15] Z. Ren, A. A. Taskin, S. Sasaki, K. Segawa, Y. Ando, *Phys. Rev. B* **2011**, *84*, 165311.
[16] Y. Zhang, Y. Ran, A. Vishwanath, *Phys. Rev. B* **2009**, *79*, 245331.
[17] J. H. Bardarson, P. W. Brouwer, J. E. Moore, *Phys. Rev. Lett.* **2010**, *105*, 156803.
[18] J. H. Bardarson, J. E. Moore, *Rep. Prog. Phys.* **2013**, *76*, 056501.
[19] H. Peng, K. Lai, D. Kong, S. Meister, Y. Chen, X.-L. Qi, S.-C. Zhang, Z.-X. Shen, Y. Cui, *Nat. Mater.* **2010**, *9*, 225.
[20] Y. Zhang, A. Vishwanath, *Phys. Rev. Lett.* **2010**, *105*, 206601.
[21] F. Xiu, L. He, Y. Wang, L. Cheng, L.-T. Chang, M. Lang, G. Huang, X. Kou, Y. Zhou, X. Jiang, Z. Chen, J. Zou, A. Shailos, K. L. Wang, *Nat. Nanotechnol.* **2011**, *6*, 216.
[22] S. Cho, B. Dellabetta, R. Zhong, J. Schneeloch, T. Liu, G. Gu, M. J. Gilbert, N. Mason, *Nat. Commun.* **2015**, *6*, 7634.
[23] L. A. Jauregui, M. T. Pettes, L. P. Rokhinson, L. Shi, Y. P. Chen, *Sci. Rep.* **2015**, *5*, 8452.
[24] Y. C. Arango, L. Huang, C. Chen, J. Avila, M. C. Asensio, D. Grützmacher, H. Lüth, J. G. Lu, Th. Schäpers, *Sci. Rep.* **2016**, *6*, 29493.
[25] K. Moors, P. Schüffelgen, D. Rosenbach, T. Schmitt, Th. Schäpers, T. L. Schmidt, *Phys. Rev. B* **2018**, *97*, 245429.
[26] P. Schüffelgen, D. Rosenbach, C. Li, T. W. Schmitt, M. Schleenvoigt, A. R. Jalil, S. Schmitt, J. Kölzer, M. Wang, B. Bennemann, U. Parlak, L. Kibkalo, S. Trellenkamp, T. Grap, D. Meertens, M. Luysberg, G. Mussler, E. Berenschot, N. Tas, A. A. Golubov, A. Brinkman, Th. Schäpers, D. Grützmacher, *Nat. Nanotechnol.* **2019**, *14*, 825.
[27] C. Weyrich, T. Merzenich, J. Kampmeier, I. E. Batov, G. Mussler, J. Schubert, D. Grützmacher, Th. Schäpers, *Appl. Phys. Lett.* **2017**, *110*, 092104.
[28] J. Kölzer, D. Rosenbach, C. Weyrich, T. W. Schmitt, M. Schleenvoigt, A. R. Jalil, P. Schüffelgen, G. Mussler, V. E. Sacksteder IV, D. Gruetzmacher, H. Lueth, Th. Schäpers, *Nanotechnology* **2020**, *31*, 325001.
[29] E. Bocquillon, *Nat. Nanotechnol.* **2019**, *14*, 815.
[30] D. O. Scanlon, P. D. C. King, R. P. Singh, A. de la Torre, S. M. Walker, G. Balakrishnan, F. Baumberger, C. R. A. Catlow, *Adv. Mater.* **2012**, *24*, 2154.
[31] G. Bergmann, *Solid State Commun.* **1982**, *42*, 815.
[32] J. Ziegler, R. Kozlovsky, C. Gorini, M.-H. Liu, S. Weishäupl, H. Maier, R. Fischer, D. A. Kozlov, Z. D. Kvon, N. Mikhailov, S. A. Dvoretsky, K. Richter, D. Weiss, *Phys. Rev. B* **2018**, *97*, 035157.
[33] M. Lang, L. He, F. Xiu, X. Yu, J. Tang, Y. Wang, X. Kou, W. Jiang, A. V. Fedorov, K. L. Wang, *ACS Nano* **2012**, *6*, 295.
[34] H. Berger, Contact resistance on diffused resistors, 1969 IEEE International Solid-State Circuits Conference. Digest of Technical Papers **1969**, *XII*, 160.
[35] G. S. Marlow, M. B. Das, *Solid State Electron.* **1982**, *25*, 91.
[36] C. Beenakker, H. van Houten, *Quantum transport in semiconductor nanostructures, in Semiconductor Heterostructures and Nanostructures, Solid State Physics*, Vol. 44, Academic Press, San Diego, CA **1991**.
[37] P. A. Lee, A. D. Stone, H. Fukuyama, *Phys. Rev. B* **1987**, *35*, 1039.
[38] C. W. J. Beenakker, H. van Houten, *Phys. Rev. B* **1988**, *37*, 6544.
[39] J. Wang, A. M. DaSilva, C.-Z. Chang, K. He, J. K. Jain, N. Samarth, X.-C. Ma, Q.-K. Xue, M. H. W. Chan, *Phys. Rev. B* **2011**, *83*, 245438.
[40] F. Lüpke, M. Eschbach, T. Heider, M. Lanius, P. Schüffelgen, D. Rosenbach, N. von den Driesch, V. Cherepanov, G. Mussler, L. Plucinski, D. Grützmacher, C. M. Schneider, B. Voigtländer, *Nat. Commun.* **2017**, *8*, 15704.
[41] S. Borisova, J. Krumrain, M. Luysberg, G. Mussler, D. Grützmacher, *Cryst. Growth Des.* **2012**, *12*, 6098.
[42] S. Borisova, J. Kampmeier, M. Luysberg, G. Mussler, D. Grützmacher, *Appl. Phys. Lett.* **2013**, *103*, 081902.
[43] The distance $l_{terrace}$ in between two out of plane steps on the Si(111) substrate can be deduced from the miscut angle of the Si(111) wafer of $\Phi = 0.08 \pm 0.02°$, as measured by x-ray diffraction, following $l_{terrace} = a_0/(\sqrt{3} \cdot tan(\Phi))$, where $a_0 = 0.543102$ nm is the lattice constant of silicon.
[44] F. Haas, T. Wenz, P. Zellekens, N. Demarina, T. Rieger, M. Lepsa, D. Grützmacher, H. Lüth, Th. Schäpers, *Sci. Rep.* **2016**, *6*, 24573.
[45] W. Zhang, R. Yu, H.-J. Zhang, X. Dai, Z. Fang, *New J. Phys.* **2010**, *12*, 065013.
[46] E. Frantzeskakis, S. V. Ramankutty, N. de Jong, Y. K. Huang, Y. Pan, A. Tytarenko, M. Radovic, N. C. Plumb, M. Shi, A. Varykhalov, A. de Visser, E. van Heumen, M. S. Golden, *Phys. Rev. X* **2017**, *7*, 041041.
[47] G. P. Mikitik, Y. V. Sharlai, *Phys. Rev. Lett.* **1999**, *82*, 2147.
[48] R. Akiyama, K. Sumida, S. Ichinokura, R. Nakanishi, A. Kimura, K. A. Kokh, O. E. Tereshchenko, S. Hasegawa, *J. Phys. Condens. Matter* **2018**, *30*, 265001.
[49] A. K. Okazaki, S. Wiedmann, S. Pezzini, M. L. Peres, P. H. O. Rappl, E. Abramof, *Phys. Rev. B* **2018**, *98*, 195136.
[50] J. Xiong, Y. Luo, Y. H. Khoo, S. Jia, R. J. Cava, N. P. Ong, *Phys. Rev. B* **2012**, *86*, 045314.
[51] M. Eschbach, *Band Structure Engineering in 3D Topological Insulators Investigated by Angle-Resolved Photoemission Spectroscopy*, Ph.D. thesis, University of Duisburg-Essen **2016**.
[52] F. Lüpke, S. Just, M. Eschbach, T. Heider, E. Młyńczak, M. Lanius, P. Schüffelgen, D. Rosenbach, N. von den Driesch, V. Cherepanov, G. Mussler, L. Plucinski, D. Grützmacher, C. M. Schneider, F. S. Tautz, B. Voigtländer, *npj Quantum Mater.* **2018**, *3*, 46.
[53] S. Barua, K. P. Rajeev, A. K. Gupta, *J. Phys.: Condens. Matter* **2014**, *27*, 015601.
[54] J. Gooth, B. Hamvdou, A. Dorn, R. Zierold, K. Nielsch, *Appl. Phys. Lett.* **2014**, *104*, 243115.
[55] J. Andzane, G. Kunakova, S. Charpentier, V. Hrkac, L. Kienle, M. Baitimirova, T. Bauch, F. Lombardi, D. Erts, *Nanoscale* **2015**, *7*, 15935.
[56] M. Tian, W. Ning, Z. Qu, H. Du, J. Wang, Y. Zhang, *Sci. Rep.* **2013**, *3*, 1212.